FULL PAPER

Monolayer MoS_2 Growth on Au Foils and On-Site Domain Boundary Imaging

Jianping Shi, Yang Yang, Yu Zhang, Donglin Ma, Wei Wei, Qingqing Ji, Yanshuo Zhang, Xiuju Song, Teng Gao, Cong Li, Xinhe Bao, Zhongfan Liu, Qiang Fu, and Yanfeng Zhang**

Controllable synthesis of large domain, high-quality monolayer MoS_2 is the basic premise both for exploring some fundamental physical issues, and for engineering its applications in nanoelectronics, optoelectronics, etc. Herein, by introducing H_2 as carrier gas, the successful synthesis of large domain monolayer MoS_2 triangular flakes on Au foils, with the edge length approaching to 80 mm is reported. The growth process is proposed to be mediated by two competitive effects with H_2 acting as both a reduction promoter for efficient sulfurization of MoO_3 and an etching reagent of resulting MoS_2 flakes. By using low-energy electron microscopy/diffraction, the crystal orientations and domain boundaries of MoS_2 flakes directly on Au foils for the first time are further identified. These on-site and transfer-free characterizations should shed light on the initial growth and the aggregation of MoS_2 on arbitrary substrates, further guiding the growth toward large domain flakes or monolayer films.

1. Introduction

Single-cell thick-layered molybdenum disulfide (MoS_2) (a member of the transition metal dichalcogenides (TMDCs)) has sparked wide interest in both basic researches and novel applications, such as optoelectronics,[1–6] valleytronics,[7–11] light absorption,[12–15] and hydrogen evolution reaction (HER),[16–19] etc. However, achieving high-quality monolayer samples is highly needed to meet the application requirements. For this, various methods such as top-down micromechanical exfoliation,[20] ionic intercalation,[21] and bottom-up transition metal sulfurization,[22,23] etc., have been employed but sometimes resulted MoS_2 flakes with unsatisfactory quality. Chemical vapor deposition (CVD) has been proven to be a promising route for synthesizing large domain high-quality monolayer TMDCs due to its high tunability in growth parameters.[24–32] So far, the CVD growth of MoS_2 are typically performed on insulating substrates (SiO_2,[33] mica,[34] sapphire,[35] and $SrTiO_3$,[36] and oriented toward optimizing the process details, such as growth temperature[30] and precursor–substrate distance, etc.[35] Despite these endeavors, many details remain unclear and require thorough explorations. In particular, the introduction of hydrogen (H_2) was reported to be effective in facilitating the growth of WS_2 and WSe_2 in separate efforts.[27,35] However, the fundamental role of H_2 in the synthesis of MoS_2 remains ambiguous and needs to be intensively explored, considering that the etching effect of H_2 has been intensively studied for the growth of centimeter-scale uniform graphene on metal substrates.[37–39]

Moreover, identifying the domain orientations and the domain boundaries of polycrystalline MoS_2 flakes is also of particular significance for understanding the domain merging process, and for guiding the growth toward large domain and uniform thickness. Transmission electron microscopy (TEM) characterization is usually employed to resolve such issues, in which a sample transfer process is commonly indispensable.[40] Photoluminescent (PL) mapping was also utilized to realize an on-site identification of the domain boundary, according to the PL yield difference between domain boundary and domain interior.[33] However, an additional charge disorder effect induced by the substrate or the surface adsorbates makes the experimental results much more complicated. Recently, a new characterization technique, namely, second harmonic generation,[41] was also introduced to image the domain boundary embedded in a continuous MoS_2 film. Briefly, searching for facile and nondestructive recognition methods is highly desired for further optimizing the growth process.

Herein, we demonstrate the controlled growth of monolayer MoS_2 flakes and continuous films on Au foils via low-pressure CVD (LPCVD), with the introduction of H_2 as carrier gas. On

Dr. J. Shi, Dr. Y. Zhang, Dr. Y. Zhang, Dr. C. Li, Prof. Y. Zhang
Department of Materials Science & Engineering
College of Engineering, Peking University
Beijing 100871, P. R. China
E-mail: yanfengzhang@pku.edu.cn
Dr. J. Shi, Dr. Y. Zhang, Dr. D. Ma, Dr. Q. Ji, Dr. Y. Zhang, Dr. X. Song, Dr. T. Gao, Dr. C. Li, Prof. Z. Liu, Prof. Y. Zhang
Center for Nanochemistry (CNC)
Beijing National Laboratory for Molecular Sciences
College of Chemistry and Molecular Engineering
Peking University
Beijing 100871, P. R. China
Dr. Y. Yang, Dr. W. Wei, Prof. X. H. Bao, Prof. Q. Fu
State Key Laboratory of Catalysis
Dalian Institute of Chemical Physics
Chinese Academy of Science
Dalian 116023, P. R. China
E-mail: qfu@dicp.ac.cn

DOI: 10.1002/adfm.201403659

one hand, the H_2 carrier gas is expected to serve as a reduction promoter for the efficient sulfurization reaction of MoO_3, which directly leads to an increased deposition rate of MoS_2 and enlarged domain size. On the other hand, H_2 is also considered to serve as an etching reagent of MoS_2 followed with shrinkage of existing domain. The two competitive effects should work concurrently to determine the crystal quality and the domain size of single-crystalline monolayer MoS_2. In particular, we applied low-energy electron microscopy/diffraction (LEEM/LEED) technique to identify the domain orientations and domain boundaries of polycrystalline MoS_2 flakes directly on Au foils, and attempt to elucidate the merging behavior at the as-grown state.

2. Results and Discussion

An LPCVD system was used for the synthesis of MoS_2 directly on Au foils by referring to previous reports,[34–36] where a large precursor–substrate distance was used to achieve uniform nucleation and nonoverlapping distribution of adjacent domains. In order to remove impurities and reconstruct the single-crystalline surface, the Au foil substrates were firstly annealed at 900 °C for 1 h under 50 standard cubic centimeters per minute (sccm) Ar and 20 sccm H_2 carrier gas. The schematic view in **Figure 1**a addresses the role of H_2, either as a reduction promoter for the efficient sulfurization of MoO_3 (via Equation I) or an etching reagent of resulting MoS_2 flakes (via forward reaction of Equation II). X-ray photoelectron spectroscopy (XPS) spectra were firstly captured to confirm the formation of MoS_2 on Au foils (Figure S1, Supporting Information). The shift of Mo $3d_{5/2}$ and S 2p peak positions to the lower binding energies probably reflects electron donation from the Au foils to the MoS_2 sheets.[42] The result is fully consistent with previous XPS studies of an inverted system of Au nanoparticles evaporated on MoS_2,[43] and in accordance with MoS_2 behaving as an n-type semiconductor on Au foils.[44]

Further scanning electron microscope (SEM) images reveal that increasing the H_2 gas flow rate from 0 to 3 sccm results in an increase of the average edge length of the triangular MoS_2 domains from ≈7.8 to 20.9 μm (Figure 1b,c and Figure S2a–d). With a further increase of H_2 flow rate to 5 and 6 sccm, the average edge length can be as large as ≈47.8 and 55.8 μm, respectively (Figure 1d,e and Figure S2e–g). Additionally, the

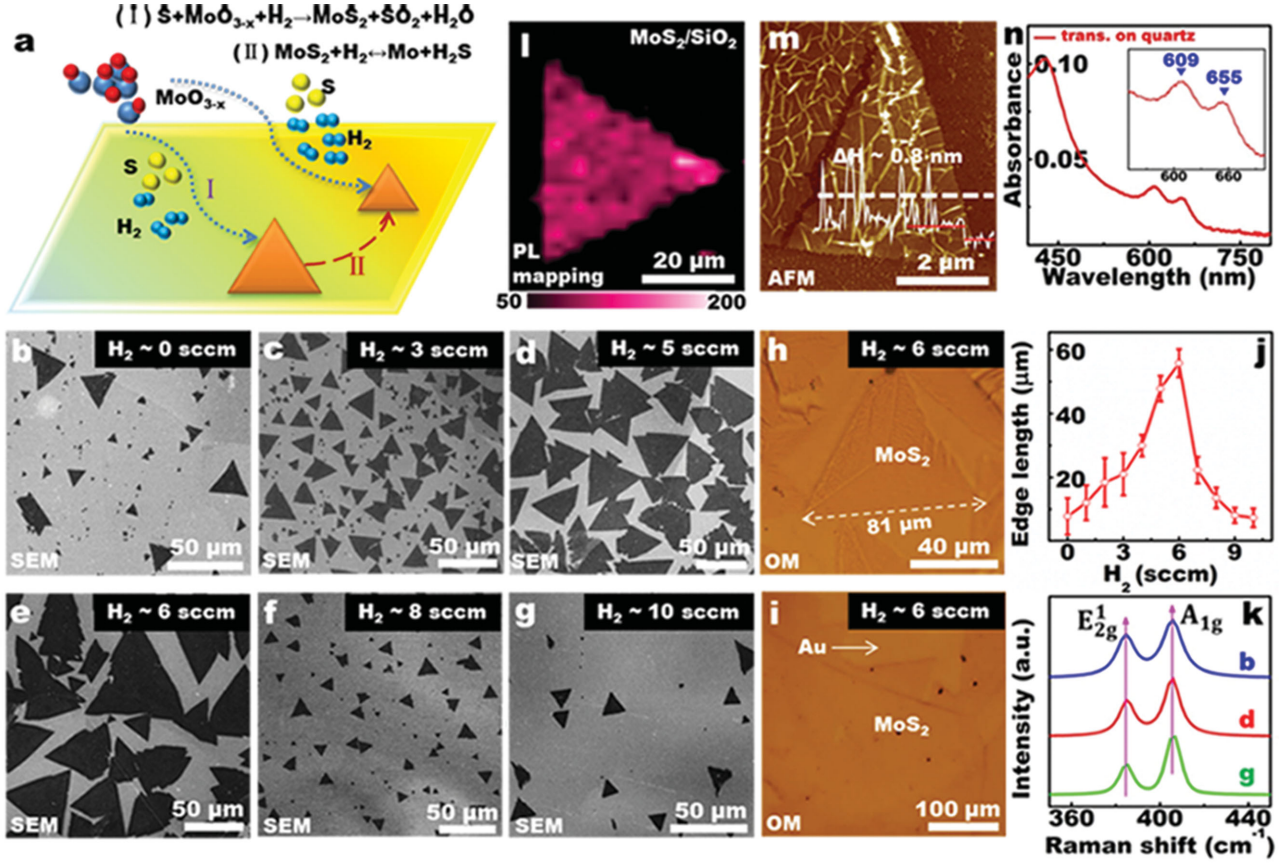

Figure 1. MoS_2 domain size variation as a function of H_2 flow rate. a) Schematic view presenting the role of H_2 in MoS_2 synthesis. b–g) SEM images of MoS_2 grown on Au foils under distinct H_2 flow rates (0–10 sccm, CVD growth for 1 h at 680 °C under 50 sccm Ar carrier gas). h,i) Optical microscope images of large domain and large area MoS_2 grown on Au foils under 6 sccm H_2. j) Statistical distribution of the edge length of triangular MoS_2 domains as a function of H_2 flow rate (statistics based on SEM images including at least 100 flakes). k) Raman spectra of MoS_2 on Au foils as shown in (b), (d), and (g) indicating their monolayer nature. l) PL mapping image of a near triangular MoS_2 domain transferred onto SiO_2/Si. m) AFM image of MoS_2 transferred on SiO_2/Si and corresponding line profile along the white-dashed line showing a monolayer thickness of ≈0.8 nm. n) UV–Vis spectra of a near complete monolayer MoS_2 film after transferred on quartz.

homogeneity of the domain size and the coverage of synthesized MoS_2 are improved accordingly throughout the flow rate range. Even larger domain flakes (edge length of ≈81 μm) and near complete MoS_2 films are available in 6 sccm H_2 (Figure 1h,i and Figure S3, Supporting Information). Particularly, the large domain MoS_2 flakes can spread cross the Au grain boundaries with their shapes and orientations nearly unchanged (Figure S3, Supporting Information), which should facilitate the growth of large domain MoS_2 on polycrystalline Au foils. Notably, with a further increase of H_2 flow rate to 8 and 10 sccm (Figure 1f,g and Figure S2h–k), the obtained MoS_2 domains start to shrink to edge lengths of ≈13.5 and ≈7.3 μm, respectively. For more details, the average edge length of MoS_2 domains as a function of H_2 flow rate is presented in Figure 1j.

In order to explain the complicated experimental results, the effect of H_2 in the CVD growth process should be considered in detail. On one hand, H_2 (at low flow rate) should serve as a reduction promoter for the efficient sulfurization of MoO_3 and the fast growth of MoS_2. And the involved chemical reaction is shown in Figure 1a (with Equation I). Meanwhile, a small quantity of H_2 is also useful for reducing the inherent oxygen-containing impurities on Au foils and decreasing the nucleation density, considering that the impurities may act as nucleation sites for MoS_2 growth.[38] The combined effects from the increased precursor supply and the reduced nucleation density should result in increased domain size and enhanced MoS_2 coverage (Figure 1c–e). On the other hand, a high H_2 flow rate is also effective in the reduction of MoO_3 to Mo metals and this may directly suppress the precursor supply and subsequent MoS_2 growth (Figure 1f,g). Meanwhile, a high H_2 flow rate is also active in etching the existing MoS_2 domains, as show in Figure 1a (forward reaction of Equation II). The etching product (Mo) may form alloys with the Au substrate at high temperature, which promotes the etching process.[45,46] Consequently, at high H_2 flow rate, the synergistic effects of reducing MoO_3 precursor supply and etching existing MoS_2 flake should work concurrently to result in reduced domain size. In this case, through an appropriate control of H_2 flow rate, large domain MoS_2 can be obtained on Au foils by a balance of the two competitive effects.

Raman spectroscopy measurements were then carried out to identify the layer thickness of as-grown MoS_2 on Au foils (Figure 1k). Two typical Raman peaks, corresponding to the out-of-plane vibration of S atoms (A_{1g}) at ≈406.9 cm^{-1} and in-plane vibration of Mo and S atoms (E1 2g) at ≈387.0 cm^{-1}, are obtained to be invariable with the H_2 flow rate. In particular, the frequency difference, $\Delta \approx 19.9$ cm^{-1}, acquired from the various samples shown in Figure 1b,d,g is in good agreement with those reported for monolayer MoS_2,[47] thereby indicating the monolayer nature of MoS_2 on Au foils under different H_2 flow rates. The growth of monolayer MoS_2 on Au foils is thus considered to obey a 2D growth feature.

In order to confirm the layer thickness and its uniformity, a chemical wet etching method was utilized to transfer as-grown MoS_2 onto arbitrary substrates like SiO_2/Si, quartz, and mica (optical microscope (OM) images in Figure S4, Supporting Information). The homogeneous PL and Raman contrasts (Figure 1l and Figure S4 (Supporting Information), respectively) convince the rather high thickness uniformity and crystal quality of the transferred MoS_2. Interestingly, a frequency difference of $\Delta \approx 18.6$ cm^{-1} between E1 2g and A_{1g} Raman modes (Figure S4, Supporting Information) can be obtained, slightly smaller than that before transfer ($\Delta \approx 19.9$ cm^{-1}). This could be explained from the release of strong interface interaction between overlayer and substrate after the sample transfer process. The measured PL peak locations are found to be in the range of 665.1–665.3 nm for MoS_2 on SiO_2, further demonstrating the high crystal quality of the synthesized MoS_2 on Au foils (Figure S4, Supporting Information). An apparent height of ≈0.8 nm obtained from the atomic force microscopy (AFM) height profile for MoS_2 on SiO_2/Si (Figure 1m) again suggests its monolayer nature.[25] A number of wrinkles, usually possessing a height of >1 nm can be noticed in Figure 1m, which are probably generated from the transfer process. UV–Vis absorption spectra of transferred monolayer MoS_2 on quartz (with a scale of 1×1 cm^2) was also collected to show two excitonic absorption bands at 655 nm (1.89 eV) and 609 nm (2.04 eV), respectively (Figure 1n). The energy difference is ≈0.15 eV, which is in good agreement with the theoretical value of 0.148 eV for monolayer MoS_2.[48] All these results consistently verify the centimeter-scale thickness uniformity and high crystal quality of monolayer MoS_2.

In order to achieve more quantitative results, the surface morphology evolution was then intensively examined under different H_2 flow rates. Interestingly, when etched with ≈12 sccm H_2 and 50 sccm Ar at 680 °C (**Figure 2**a), the edge length and shape of MoS_2 flakes on Au foils varies prominently with increasing etching time from 10 to 30 min. Accordingly, the domain size and coverage noticeably decrease, along with a sharp transition of the flake shape from near triangles to truncated triangles (Figure 2b–d). Notably, small MoS_2 domains seem more vulnerable to the etching process than those larger ones, since they can be etched away within 5–10 min. Further increasing the H_2 flow rate to ≈15 sccm can induce a quick etching of MoS_2 flakes, as similarly presented in Figure 2e–h. Considering the high catalytic activity of Au in the dissociation of H_2 to form active atomic H at high temperature,[49] it is suggested that the atomic H species should play a significant role in etching existing MoS_2 synthesized on Au foils.

The edge length evolution of monolayer MoS_2 flakes as a function of etching time was then plotted in Figure 2i, where a nearly linear behavior is obtained after that the smaller domains are etched away. The etching rates (in edge length) are then calculated to be 1.44 and 2.16 μm min^{-1} for 12 and 15 sccm of H_2 flow rates, respectively. In order to attain a further understanding of the surface chemical reactions, XPS spectra of MoS_2 samples before and after etching processes are presented in Figure 2j–l, respectively. The two Mo 3d peaks (located at 235.2 ($3d_{3/2}$) and 232.1 eV ($3d_{5/2}$)) for etched samples are obviously blue shifted with respect to those before etching ($3d_{3/2}$:232.3 eV; $3d_{5/2}$:229.1 eV), which probably arises from a charge transfer effect between Mo and Au atoms via the formation of Mo–Au alloy at 680 °C.[50] To sum up, H_2 etching process is effective in decreasing the nucleation density, and tuning the flake shape of MoS_2 on Au foils.

In addition to universally visible triangular MoS_2 flakes, more complicated shapes, e.g., stars and butterfly like shapes are also observable (**Figure 3**a,b). Some particles that arise from the incomplete sulfurization of suboxide species (MoO_{3-x}) were sometimes observed either on Au substrates or on MoS_2 flakes.

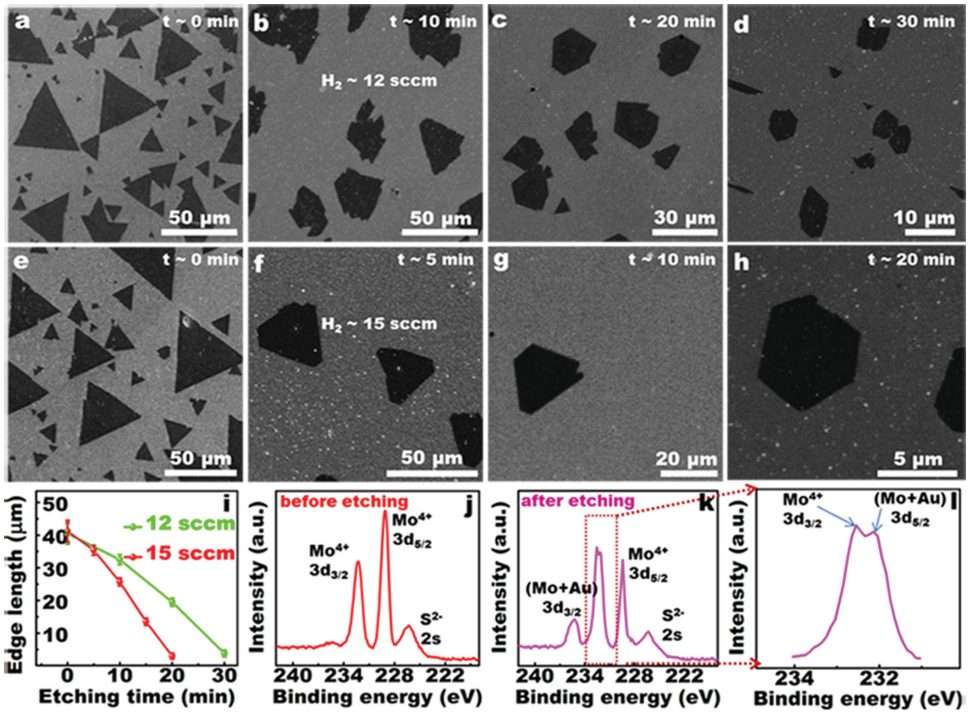

Figure 2. Domain size and shape evolution of existing MoS_2 on Au foils during the H_2 etching process. a) SEM image of as-grown MoS_2 flakes on Au foils (growth for 1 h at 680 °C under 50 sccm Ar and 3 sccm H_2 carrier gas). b–d) SEM images showing the morphology evolution of MoS_2 flakes processed with a gas flow of 50 sccm Ar and 12 sccm H_2 at 680 °C for (b) ≈10 min, (c) ≈20 min, and (d) ≈30 min, respectively. e) Similar as-grown monolayer MoS_2 flakes on Au foils as that of (a). f–h) SEM images showing the etched MoS_2 domains by a gas flow of 50 sccm Ar and 15 sccm H_2 at 680 °C for (f) ≈5 min, (g) ≈10 min, and (h) ≈20 min, respectively. i) Edge length evolution of near triangular MoS_2 flakes with etching time (statistics are based on SEM images including at least tens of MoS_2 domains). j–k) XPS spectra of MoS_2 on Au foils before and after etching process, respectively. l) Expanded data of (k) showing the formation of Au–Mo alloys.

And these particles can be removed by sample annealing at high temperature (800 °C) in S vapor atmosphere. Intriguingly, the domain boundary of the triangular aggregate was recently detected to have mid-gap metallic modes that may enhance the catalytic activity for HER.[51] Hereby, imaging the domain boundaries and exploring their formation mechanism become essential for further enlarging the domain size and for understanding the HER performance. As-grown MoS_2 flakes were then transferred onto carbon films supported on copper grids for TEM characterizations by referring to previous reports.[33,40] Note that the single-crystalline and Mo-terminated features of a near triangular flake can be definitely deduced from related TEM characterizations.[33]

Besides single-crystalline triangles, a polygonal MoS_2 flake merged by two-aligned triangles was also imaged by bright-field TEM (BF-TEM) (Figure 3c). Corresponding selective area electron diffraction (SAED) pattern shows only one set of hexagonally arranged diffraction spots, highly suggestive of the parallel orientation of the merged triangles (Figure 3d). The color-coded overlay of the dark-field TEM (DF-TEM) image (Figure 3e) according to the diffraction spots in Figure 3d reconfirms the same orientation of the two-merged flakes. In contrast, Figure 3f shows the BF-TEM image of two-merged MoS_2 triangles rotated by 180° with respect to each other. The corresponding SAED pattern (Figure 3g) also reveals only one set of hexagonally arranged diffraction spots, which can be attributed to the perfect mirror symmetric merging of the two MoS_2 triangles. The color-coded overlay of the DF-TEM image (Figure 3h) corresponding to the diffraction spots in Figure 3g again indicates the same orientation of the composite domains.

In contrast, Figure 3i presents two MoS_2 triangles rotated by ≈27° with each other, as convinced by corresponding SAED pattern showing two sets of hexagonally arranged diffraction spots (Figure 3j). Similar color-coded DF-TEM image (Figure 3k) demonstrates the rotated orientation of the two triangles, as well as their merging boundaries. It is worthy of mentioning that after transferred onto the TEM grids, the merged flake is almost crack from the domain boundary, which is probably mediated by a nonuniform strain relaxation at the domain boundary throughout the sample transfer process.

Although identifying the domain boundary of polycrystalline MoS_2 has received comprehensive studies through TEM characterizations,[30,33,36,40] the inevitable sample transfer process usually induces impurity adsorption or flake cracking at the domain boundary. In this regard, it should be highly desired to develop some on-site imaging methods. LEEM is a unique characterization tool, which is capable of performing structural measurements and revealing the crystalline quality and orientation of solid surfaces.[52–56] In view of the conductive nature of MoS_2/Au foils, LEEM was then introduced to image a MoS_2 triangle directly (**Figure 4**a). The crystalline structure of the triangle was investigated by microregion LEED (μ-LEED), which complemented real-space images due

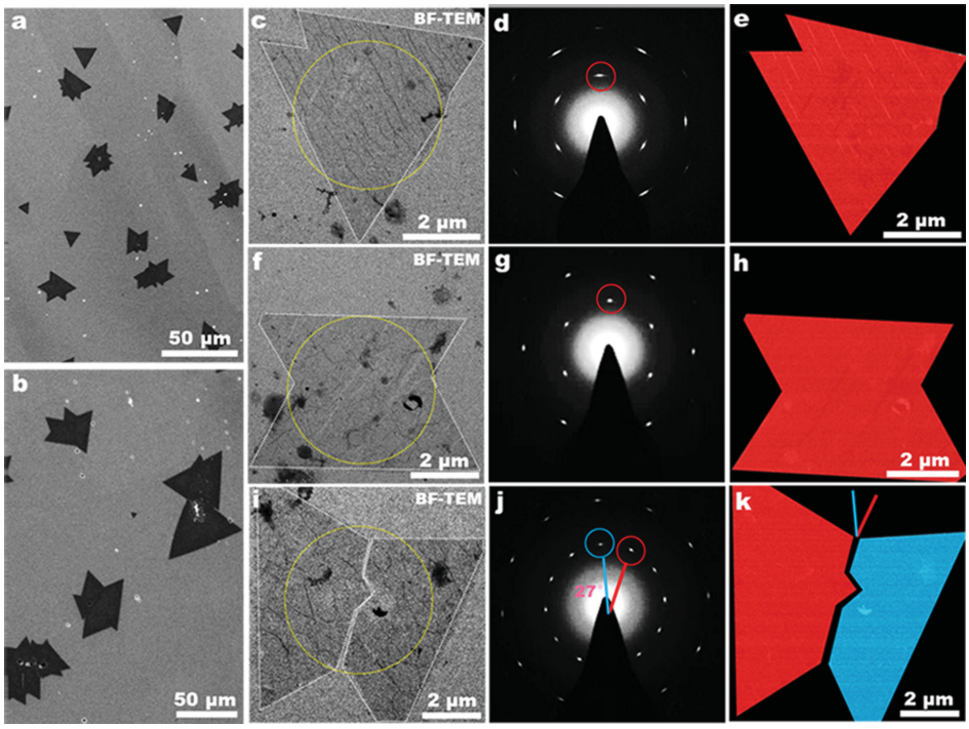

Figure 3. TEM characterization of the relative orientations of aggregated monolayer MoS_2 triangles transferred onto carbon films supported on copper grids. a,b) SEM images of polygonal MoS_2 flakes on Au foils. c) BF-TEM image of a polygonal MoS_2 flake merged by two-aligned triangles. d) Corresponding SAED pattern for (c) (selected area marked by the superimposed circle). e) Color-coded overlay of the DF-TEM image according to the diffraction spot in (d). f) BF-TEM image of a mirror twin composed of 180°-rotated triangles. g) Corresponding SAED pattern taken from the area marked by the circle in (f). h) Color-coded overlay of the DF-TEM image according to the diffraction spot in (g). i) BF-TEM image of two triangles with an intersection angle and broken merging boundary. j) Corresponding SAED pattern for (i) showing a 27° misorientation of the two domains (measured between the red and cyan lines). k) Color-coded overlay of the DF-TEM image corresponding to the red- and cyan-circled spots in (j).

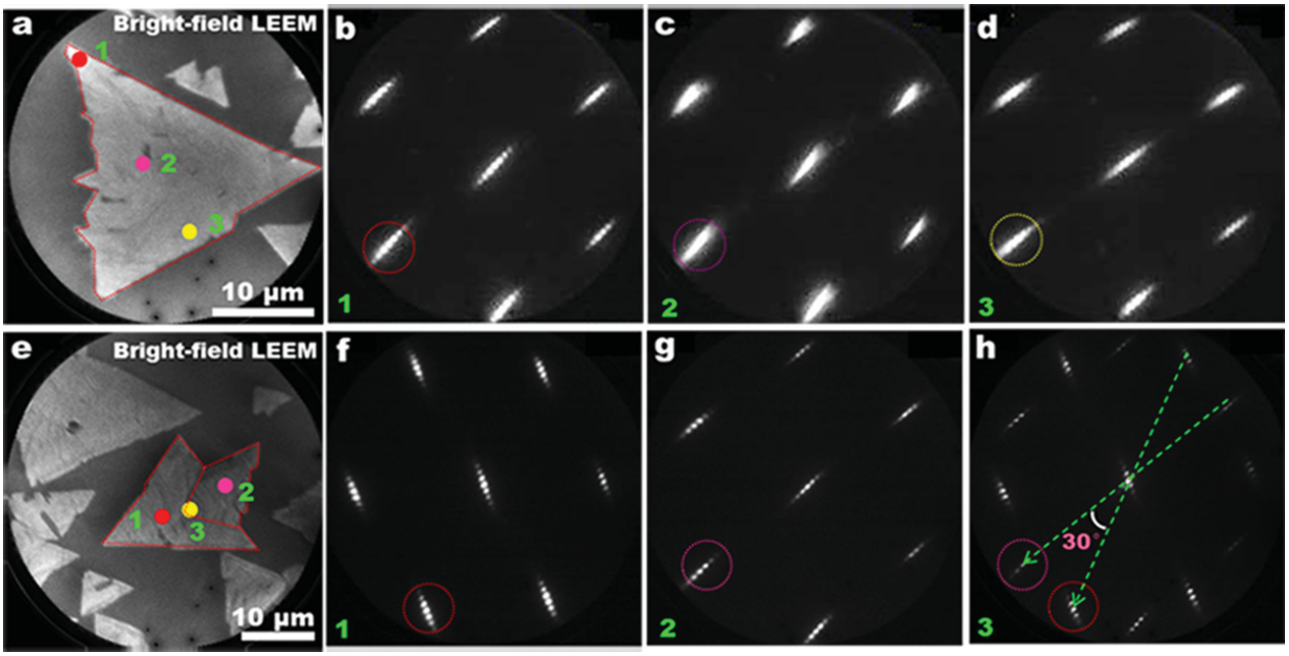

Figure 4. LEEM and μ-LEED characterizations of the crystal orientations of MoS_2 grown on Au foils. a) LEEM image (at 3.9 eV) of a monolayer MoS_2 triangle on Au foils. b–d) LEED patterns (48 eV) taken from the regions indicated by the red (1), pink (2), and yellow (3) dots in (a). e) LEEM image (at 4.5 eV) of a polygonal MoS_2 flake (circled by dashed line) merged by two islands with an overlapping edge. f–h) LEED patterns (48 eV) taken from the composite domains and the domain boundary, indicated by the red (1), pink (2), and yellow (3) dots in (**e**), respectively.

to its sensitivity to the crystal deformation on length scales from ≈20 nm to interatomic distances.[52] LEED patterns acquired from three typical positions indicated by the dots (1, 2, and 3, in line with corner, center, and edge sites) in Figure 4a present an identical lattice orientation (Figure 4b–d). This hereby indicates a single-crystal nature of this triangle, as similarly revealed by TEM characterizations. Nevertheless, the nondestructive characterization techniques of LEEM/LEED are well suitable for high-throughput analysis of the crystal structure of MoS_2.

The LEEM image of a polygonal MoS_2 flake, which is merged by two domains with one flake locating at the edge of the other one, is presented in Figure 4e. The corresponding LEED patterns taken from the two domains and their merging boundary (indicated by red (1), pink (2), and yellow (3) dots in Figure 4e) are shown in Figure 4f–h, respectively. It is noteworthy that the large and small domains present different lattice orientations with each other, and the pattern from the merging boundary reveals two sets of diffraction spots with an angle difference of ≈30°. Consequently, by virtue of bright-field LEEM (BF-LEEM) image and LEED pattern, the crystalline orientations of aggregated flakes can be tentatively defined.

LEEM characterization of a monolayer MoS_2 aggregate composed by two-aligned triangles was then performed directly on Au foils. Corresponding LEED pattern recorded from the probable domain boundary (indicated by the red dot in **Figure 5**a) presents only one set of pattern (Figure 5b), suggesting the same lattice orientation of the two-merged MoS_2 domains. Further dark-field LEEM (DF-LEEM) image obtained according to the spot indicated by the red circle in Figure 5b, displays uniform contrast over the merged triangles, which reconfirms the high crystalline quality and their aligned orientation (Figure 5c). Otherwise, no obvious domain boundary can be noticed from the DF-LEEM image. It is clear to see that the on-site LEEM data of MoS_2 on Au foils agree well with those of DF-TEM on transferred samples (Figure 3c–e).

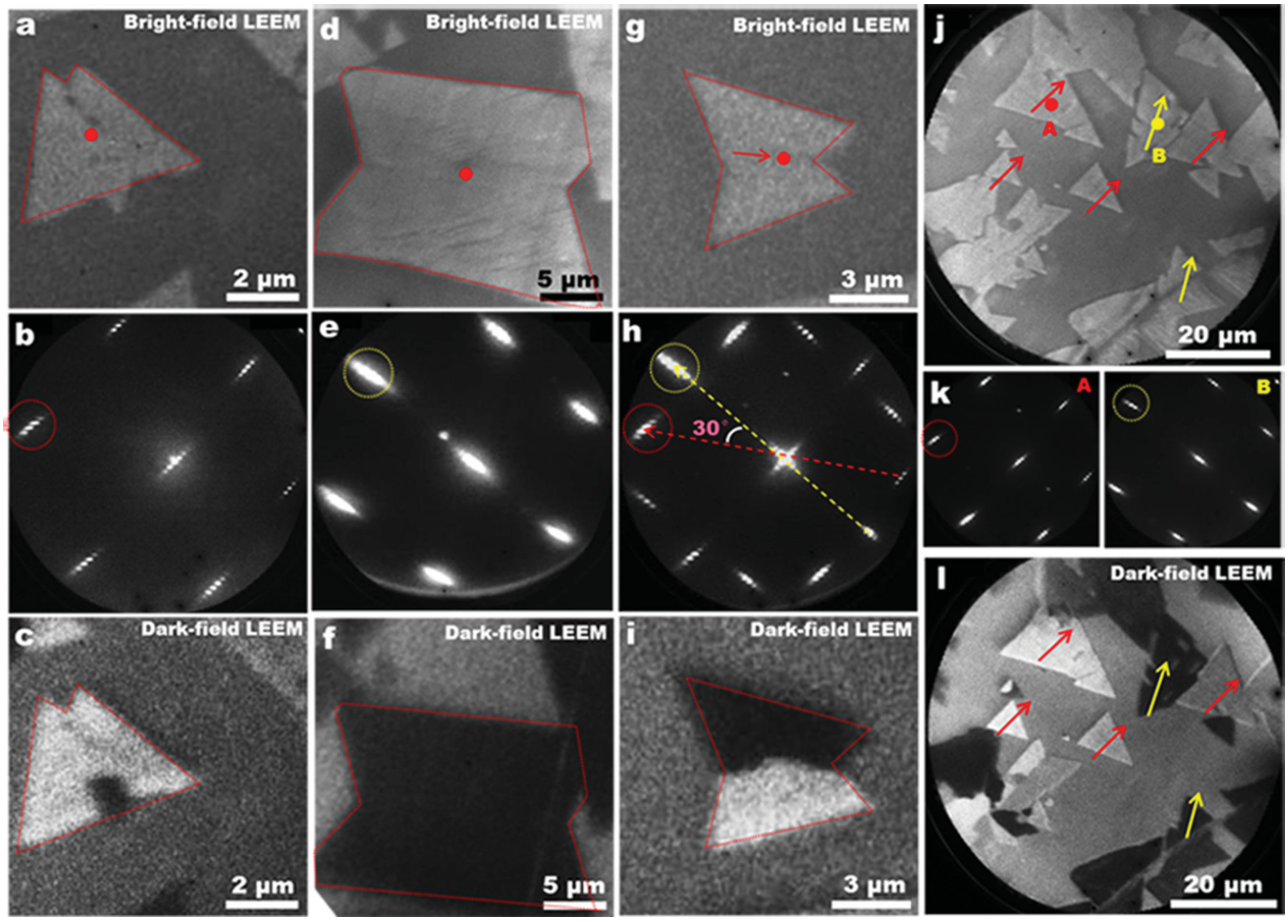

Figure 5. Merging boundary identification of polygonal monolayer MoS_2 flakes by DF-LEEM. a) BF-LEEM image (at 4.7 eV) of two-merged MoS_2 triangles with a parallel orientation. b) LEED pattern (48 eV) taken from the merging boundary indicated by the red dot in (a). c) DF-LEEM image taken from the similar area in (a) according to the LEED spot indicated by the red circle in (b). d) BF-LEEM image (at 4.7 eV) of a mirror twin composed of 180°-rotated triangles. e) LEED pattern (48 eV) taken from the merging region indicated by the red dot in (d). f) DF-LEEM image captured from the similar area in (d) according to the LEED spot indicated by the red circle in (b). g) BF-LEEM image (at 4.7 eV) of two-merged MoS_2 triangles with an intersection angle. A probable boundary is indicated by a red arrow. h) LEED pattern (48 eV) taken from the merging boundary location as indicated by a red dot in (g). i) DF-LEEM image from the similar area in image (g) obtained using the LEED spot indicated by the red circle in (h). j) Low-magnification LEEM image (at 3.9 eV) of discrete MoS_2 domains on Au foils. k) LEED patterns (48 eV) taken from single-crystalline MoS_2 domains indicated by the red (A) and yellow (B) dots in (j). l) DF-LEEM image according to the LEED pattern indicated by the red circle in (k).

As another example, Figure 5d shows the BF-LEEM image of a mirror twin composed of 180°-rotated triangles. Corresponding LEED pattern recorded from the probable domain boundary (indicated by the red dot in Figure 5d), shows only one set of LEED pattern (Figure 5e). Further DF-LEEM image obtained according to the spot indicated by the red circle in Figure 5b, manifests no obvious contrast difference through the whole polygon (Figure 5f), which indicates the aligned orientation of the two-merged MoS_2 domains. Interestingly, no clear domain boundary can be noticed from the DF-LEEM image. This result shows perfect coincidence with DF-TEM and SAED pattern analysis (Figure 3g,h).

However, the LEED pattern (Figure 5h), acquired from two-merged domains with an intersection angle (BF-LEEM image in Figure 5g), presents diffraction spots rotated by ≈30° with respect to each other. The corresponding DF-LEEM image, obtained using the spot marked by the red row in Figure 5h, reveals bright contrast for only left half of the flake, while with the other part in dark (Figure 5i). In this case, the domain boundary of the merged flakes can be clearly identified to be a folded line. It is noteworthy that the joint LEEM/μ-LEED method should be a rather reliable one in imaging the domain boundary of as-grown polygonal MoS_2 on Au foils. This differs from that of TEM/SAED which usually involves with a sample transfer process, probably causing domain boundary broken in prior to the imaging process. More LEEM/LEED characterizations of the polygonal MoS_2 domains are described in Supporting Information Figures S5 and S6.

A low-magnification LEEM image covering several discrete MoS_2 domains on Au foils is also presented in Figure 5j. Corresponding LEED patterns (Figure 5k) were then achieved from the single-crystalline MoS_2 domains indicated by red (A) and yellow (B) dots in Figure 5j. Those are actually in parallel with two types of domains with different edge orientations. DF-LEEM was then carried out according to the LEED pattern indicated by the red circle in Figure 5k (left panel). It is interesting to find that the triangular flakes with parallel edges usually have the same color contrast (Figure 5l), and thus the same lattice orientation. Hereby, the relative orientations of amount of MoS_2 domains can be efficiently differentiated in large-scale DF-LEEM images.

Based on these LEEM/LEED analyses, it can be concluded that parallel-edged or aligned MoS_2 triangles usually present the same lattice orientation, which makes them probable for merging into large single-crystalline MoS_2 domains, regardless of their different nucleation sites. However, individual islands with an intersection angle will not merge into single-crystalline flakes. DF-LEEM and μ-LEED can be used as a convenient and nondestructive characterization method for on-site, high-throughput imaging of the domain boundary, crystal orientation, and merging process of as-grown MoS_2 flakes on Au foils.

3. Conclusions

In summary, we have achieved uniform large domain triangular flakes and monolayer MoS_2 films on Au foils through introducing H_2 carrier gas. The influence of H_2 on the growth is delicately illustrated as competitively promoting and etching reagent for the CVD-growth MoS_2. Moreover, LEEM/μ-LEED was proved to be a convenient and nondestructive method for high-throughput, on-site imaging of relative orientations and domain boundaries of polycrystalline MoS_2 flakes. These results contribute greatly to elucidate their merging behavior on Au foils. Although performed on Au foils, this work should serve as a fundamental reference for understanding the growth of other TMDCs on various commonly used insulating substrates.

4. Experimental Section

Monolayer MoS_2 Growth and Transfer: An LPCVD system was used for the growth of MoS_2 on Au foils, which was composed by a multitemperature zone tubular furnace (Lindberg/Blue M) equipped with a 1 in. diameter quartz tube. Sulfur powder (Alfa Aesar, purity 99.5%), placed outside the hot zone, was mildly sublimated at ≈102 °C with heating belts, and carried by Ar and H_2 gas (50 sccm for Ar and various of H_2 flow rates from 0 to 10 sccm, the pressure of the system was changed from 10 to 23 Pa during the growth process), to the downstream growth zone. MoO_3 powder (Alfa Aesar, purity 99.9%) and Au foils (Alfa Aesar, purity 99.985%, thickness ≈25 μm) were successively placed on the downstream region of the quartz tube. By placing a heat insulator between MoO_3 powder and Au foil substrate, the vaporization temperature (of MoO_3) and the deposition temperature (of MoS_2) can be controlled, separately. The MoO_3 powder was heated from room temperature to ≈530 °C within 30 min along with a heating rate of ≈17 °C min^{-1}, and the Au foil substrate was heated to ≈680 °C within 30 min along with a heating rate of ≈20 °C min^{-1}. The growth time was set at 60 min for all the samples. To transfer as-grown MoS_2 films, the MoS_2/Au sample was firstly coated with polymethylmethacrylate (PMMA) by spin coating at 3000 rpm for 60 s, and then baked at 170 °C for 10 min. Secondly, the PMMA-coated sample was then etched in Au etchant (KI/I_2) to remove the backside Au. Finally, the PMMA-supported MoS_2 was fished out by a fresh SiO_2/Si (or other substrate) followed with annealing on a hotplate at 150 °C for 10 min to remove water and immersing in acetone bath for 5 min to remove the capping PMMA.

Characterizations of MoS_2: The prepared MoS_2 flakes were systematically characterized through optical microscopy (Olympus DX51), Raman spectroscopy (Horiba, LabRAM HR-800, excitation light ≈514 nm), SEM (Hitachi S-4800, acceleration voltage of 1–5 kV), XPS (Kratos, Axis Ultra, Mg K_α as the excitation source), PL (Horiba, LabRAM HR-800, excitation light of 514 nm in wavelength), AFM (Vecco Nanoscope III), TEM (Tecnai T20; acceleration voltage of 200 kV), and LEEM/μ-LEED (Elmitec LEEM-III system having ultrahigh vacuum of $\approx 1 \times 10^{-10}$ Torr).

Supporting Information

Supporting Information is available from the Wiley Online Library or from the author.

Acknowledgments

This work was financially supported by the National Natural Science Foundation of China (Grants Nos. 51222201, 51290272, 21201012, 51121091, 51072004, and 21222305) and the Ministry of Science and Technology of China (Grants Nos. 2011CB921903, 2012CB921404, 2012CB933404, 2013CB932603, and 2011CB933003).

Received: October 20, 2014
Revised: November 15, 2014
Published online: December 15, 2014

[1] A. Geim, I. Grigorieva, *Nature* **2013**, *499*, 419.
[2] Q. H. Wang, K. Kalantar-Zadeh, A. Kis, J. N. Coleman, M. S. Strano, *Nat. Nanotechnol.* **2012**, *7*, 699.
[3] O. Lopez-Sanchez, D. Lembke, M. Kayci, A. Radenovic, A. Kis, *Nat. Nanotechnol.* **2013**, *8*, 497.
[4] K. F. Mak, C. Lee, J. Hone, J. Shan, T. F. Heinz, *Phys. Rev. Lett.* **2010**, *105*, 136805.
[5] K. F. Mak, K. He, C. Lee, G. H. Lee, J. Hone, T. F. Heinz, J. Shan, *Nat. Mater.* **2013**, *12*, 207.
[6] A. Splendiani, L. Sun, Y. Zhang, T. Li, J. Kim, C.-Y. Chim, G. Galli, F. Wang, *Nano Lett.* **2010**, *10*, 1271.
[7] K. F. Mak, K. L. McGill, J. Park, P. L. McEuen, *Science* **2014**, *27*, 1489.
[8] H. Zeng, J. Dai, W. Yao, D. Xiao, X. Cui, *Nat. Nanotechnol.* **2012**, *7*, 490.
[9] K. F. Mak, K. He, J. Shan, T. F. Heinz, *Nat. Nanotechnol.* **2012**, *7*, 494.
[10] T. Cao, G. Wang, W. Han, H. Ye, C. Zhu, J. Shi, Q. Niu, P. Tan, E. Wang, B. Liu, J. Feng, *Nat. Commun.* **2012**, *3*, 887.
[11] S. Wu, J. S. Ross, G.-B. Liu, G. Aivazian, A. Jones, Z. Fei, W. Zhu, D. Xiao, W. Yao, D. Cobden, X. Xu, *Nat. Phys.* **2013**, *9*, 149.
[12] L. Britnell, R. Ribeiro, A. Eckmann, R. Jalil, B. Belle, A. Mishchenko, Y.-J. Kim, R. Gorbachev, T. Georgiou, S. Morozov, A. Grigorenko, A. Geim, C. Casiraghi, A. Castro Neto, K. Novoselov, *Science* **2013**, *340*, 1311.
[13] M. Bernardi, M. Palummo, J. C. Grossman, *Nano Lett.* **2013**, *13*, 3664.
[14] J. Feng, X. Qian, C.-W. Huang, J. Li, *Nat. Photonics* **2012**, *6*, 866.
[15] W. Choi, M. Y. Cho, A. Konar, J. H. Lee, G. B. Cha, S. C. Hong, S. Kim, J. Kim, D. Jena, J. Joo, S. Kim, *Adv. Mater.* **2012**, *24*, 5832.
[16] T. F. Jaramillo, K. P. Jørgensen, J. Bonde, J. H. Nielsen, S. Horch, I. Chorkendorff, *Science* **2007**, *317*, 100.
[17] J. Kibsgaard, Z. Chen, B. N. Reinecke, T. F. Jaramillo, *Nat. Mater.* **2012**, *11*, 963.
[18] M. Chhowalla, H. S. Shin, G. Eda, L.-J. Li, K. P. Loh, H. Zhang, *Nat. Chem.* **2013**, *5*, 263.
[19] X. Huang, Z. Zeng, S. Bao, M. Wang, X. Qi, Z. Fan, H. Zhang, *Nat. Commun.* **2013**, *4*, 1444.
[20] C. Lee, H. Yan, L. E. Brus, T. F. Heinz, J. Hone, S. Ryu, *ACS Nano* **2010**, *4*, 2695.
[21] J. N. Coleman, M. Lotya, A. O'Neill, S. D. Bergin, P. J. King, U. Khan, K. Young, A. Gaucher, S. De, R. J. Smith, I. V. Shvets, S. K. Arora, G. Stanton, H. Y. Kim, K. Lee, G. T. Kim, G. S. Duesberg, T. Hallam, J. J. Boland, J. J. Wang, J. F. Donegan, J. C. Grunlan, G. Moriarty, A. Shmeliov, R. J. Nicholls, J. M. Perkins, E. M. Grieveson, K. Theuwissen, D. W. McComb, P. D. Nellist, V. Nicolosi, *Science* **2011**, *331*, 568.
[22] K.-K. Liu, W. Zhang, Y.-H. Lee, Y.-C. Lin, M.-T. Chang, C.-Y. Su, C.-S. Chang, H. Li, Y. Shi, H. Zhang, C.-S. Lai, L.-J. Li, *Nano Lett.* **2012**, *12*, 1538.
[23] S. Helveg, J. V. Lauritsen, E. Lægsgaard, I. Stensgaard, J. K. Nørskov, B. Clausen, H. Topsøe, F. Besenbacher, *Phys. Rev. Lett.* **2000**, *84*, 951.
[24] Y. Shi, W. Zhou, A.-Y. Lu, W. Fang, Y.-H. Lee, A. L. Hsu, S. M. Kim, K. K. Kim, H. Y. Yang, L.-J. Li, J.-C. Idrobo, J. Kong, *Nano Lett.* **2012**, *12*, 2784.
[25] X. Wang, H. Feng, Y. Wu, L. Jiao, *J. Am. Chem. Soc.* **2013**, *135*, 5304.
[26] Y. H. Lee, X. Q. Zhang, W. Zhang, M. T. Chang, C. T. Lin, K. D. Chang, Y. C. Yu, J. T. W. Wang, C. S. Chang, L. J. Li, T.-W. Lin, *Adv. Mater.* **2012**, *24*, 2320.
[27] J.-K. Huang, J. Pu, C.-L. Hsu, M.-H. Chiu, Z.-Y. Juang, Y.-H. Chang, W.-H. Chang, Y. Iwasa, T. Takenobu, L.-J. Li, *ACS Nano* **2013**, *8*, 923.
[28] W. Zhang, J. K. Huang, C. H. Chen, Y. H. Chang, Y. J. Cheng, L. J. Li, *Adv. Mater.* **2013**, *25*, 3456.
[29] X. Ling, Y.-H. Lee, Y. Lin, W. Fang, L. Yu, M. S. Dresselhaus, J. Kong, *Nano Lett.* **2014**, *14*, 464.
[30] S. Najmaei, Z. Liu, W. Zhou, X. Zou, G. Shi, S. Lei, B. I. Yakobson, J.-C. Idrobo, P. M. Ajayan, J. Lou, *Nat. Mater.* **2013**, *12*, 754.
[31] Y. H. Chang, C. Te. Lin, T. Y. Chen, C. L. Hsu, Y. H. Lee, W. J. Zhang, K. H. Wei, L. J. Li, *Adv. Mater.* **2013**, *25*, 756.
[32] Y. H. Chang, F. Y. Wu, T. Y. Chen, C. L. Hsu, C. H. Chen, F. Wiryo, K. H. Wei, C. Y. Chiang, L. J. Li, *Small* **2014**, *10*, 895.
[33] A. M. van der Zande, P. Y. Huang, D. A. Chenet, T. C. Berkelbach, Y. You, G.-H. Lee, T. F. Heinz, D. R. Reichman, D. A. Muller, J. C. Hone, *Nat. Mater.* **2013**, *12*, 554.
[34] Q. Ji, Y. Zhang, T. Gao, Y. Zhang, D. Ma, M. Liu, Y. Chen, X. Qiao, P.-H. Tan, M. Kan, J. Feng, Q. Sun, Z. Liu, *Nano Lett.* **2013**, *13*, 3870.
[35] Y. Zhang, Y. Zhang, Q. Ji, J. Ju, H. Yuan, J. Shi, T. Gao, D. Ma, M. Liu, Y. Chen, X. Song, H. Y. Hwang, Y. Cui, Z. Liu, *ACS Nano* **2013**, *7*, 8963.
[36] Y. Zhang, Q. Ji, G.-F. Han, J. Ju, J. Shi, D. Ma, J. Sun, Y. Zhang, M. Li, X.-Y. Lang, Y. Zhang, Z. Liu, *ACS Nano* **2014**, *8*, 8617.
[37] D. Geng, B. Wu, Y. Guo, B. Luo, Y. Xue, J. Chen, G. Yu, Y. Liu, *J. Am. Chem. Soc.* **2013**, *135*, 6431.
[38] I. Vlassiouk, M. Regmi, P. Fulvio, S. Dai, P. Datskos, G. Eres, S. Smirnov, *ACS Nano* **2011**, *5*, 6069.
[39] T. Ma, W. Ren, X. Zhang, Z. Liu, Y. Gao, L.-C. Yin, X.-L. Ma, F. Ding, H.-M. Cheng, *Proc. Natl. Acad. Sci. U.S.A.* **2013**, *110*, 20386.
[40] J. Zhang, H. Yu, W. Chen, X. Tian, D. Liu, M. Cheng, G. Xie, W. Yang, R. Yang, X. Bai, D. Shi, G. Zhang, *ACS Nano* **2014**, *8*, 6024.
[41] X. Yin, Z. Ye, D. A. Chenet, Y. Ye, K. O'Brien, J. C. Hone, X. Zhang, *Science* **2014**, *344*, 488.
[42] S. Mattila, J. Leiro, M. Heinonen, T. Laiho, *Surf. Sci.* **2006**, *600*, 5168.
[43] Y. Shi, J.-K. Huang, L. Jin, Y.-T. Hsu, S. F. Yu, L.-J. Li, H. Y. Yang, *Sci. Rep.* **2013**, *3*, 1839.
[44] M. Fontana, T. Deppe, A. K. Boyd, M. Rinzan, A. Y. Liu, M. Paranjape, P. Barbara, *Sci. Rep.* **2013**, *3*, 1634.
[45] A. Christensen, A. Ruban, P. Stoltze, K. W. Jacobsen, H. L. Skriver, J. K. Nørskov, F. Besenbacher, *Phys. Rev. B* **1997**, *56*, 5822.
[46] S. G. Sørensen, H. G. Füchtbauer, A. K. Tuxen, A. S. Walton, J. V. Lauritsen, *ACS Nano* **2014**, *8*, 6788.
[47] Y. Zhao, X. Luo, H. Li, J. Zhang, P. T. Araujo, C. K. Gan, J. Wu, H. Zhang, S. Y. Quek, M. S. Dresselhaus, Q , Xiong, *Nano Lett.* **2013**, *13*, 1007.
[48] E. Bauer, J. H. van der Merwe, *Phys. Rev. B* **1986**, *33*, 3657.
[49] S. Mukherjee, F. Libisch, N. Large, O. Neumann, L. V. Brown, J. Cheng, J. B. Lassiter, E. A. Carter, P. Nordlander, N. J. Halas, *Nano Lett.* **2012**, *13*, 240.
[50] I. Song, C. Park, M. Hong, J. Baik, H. J. Shin, H. C. Choi, *Angew. Chem. Int. Ed.* **2014**, *53*, 1266.
[51] H. Liu, L. Jiao, F. Yang, Y. Cai, X. Wu, W. Ho, C. Gao, J. Jia, N. Wang, H. Fan, W. Yao, M. Xie, *Phys. Rev. Lett.* **2014**, *113*, 066105.
[52] P.-C. Yeh, W. Jin, N. Zaki, D. Zhang, J. T. Sadowski, A. Al-Mahboob, A. M. van der Zande, D. A. Chenet, J. I. Dadap, I. P. Herman, P. Sutter, J. Hone, R. M. Osgood, *Phys. Rev. B* **2014**, *89*, 155408.
[53] L. Gao, W. Ren, H. Xu, L. Jin, Z. Wang, T. Ma, L.-P. Ma, Z. Zhang, Q. Fu, L.-M. Peng, X. Bao, H.-M. Cheng, *Nat. Commun.* **2012**, *3*, 699.
[54] R. Mu, Q. Fu, L. Jin, L. Yu, G. Fang, D. Tan, X. Bao, *Angew. Chem. Int. Ed.* **2012**, *51*, 4856.
[55] D. Deng, L. Yu, X. Chen, G. Wang, L. Jin, X. Pan, J. Deng, G. Sun, X. Bao, *Angew. Chem. Int. Ed.* **2013**, *52*, 371.
[56] Y. Cui, J. Gao, L. Jin, J. Zhao, D. Tan, Q. Fu, X. Bao, *Nano Res.* **2012**, *5*, 352.